Nano Research Energy

ISSN 2791-0091 (print); 2790-8119 (online)
https://doi.org/10.26599/NRE.2026.9120260

Research Article

Controllable phosphidation engineering of $Co_2P_2O_7$@CoP core-shell electrodes for enhanced sulfur-iodine flow batteries

Jingwen Zhang[1,2,§], Jin Zhang[1,§], Renyi Wei[2,§], Xiaoyang Cheng[2] (✉), Longchao Zhuo[3], Jia He[4] (✉), and Xijun Liu[2] (✉)

[1] *School of Public Health/Key Laboratory of Endemic and Ethnic Diseases, Ministry of Education & Key Laboratory of Medical Molecular Biology of Guizhou Province, Guizhou Medical University, Guiyang 561113, China*
[2] *MOE Key Laboratory of New Processing Technology for Nonferrous Metals and Materials, Guangxi Key Laboratory of Processing for Non-ferrous Metals and Featured Materials, School of Resources, Environment and Materials, Guangxi University, Nanning 530004, China*
[3] *School of Materials Science and Engineering, Xi'an University of Technology, Xi'an 710048, China*
[4] *Institute for Advanced Interdisciplinary Research (iAIR), University of Jinan, Jinan 250022, China*
§ *Jingwen Zhang, Jin Zhang, and Renyi Wei contributed equally to this work.*

Received: 9 July 2026 / **Revised:** 21 July 2026 / **Accepted:** 29 July 2026 / **Published date:** 25 August 2026

ABSTRACT

Polysulfide/iodide redox flow batteries (SIFBs) are promising for large-scale energy storage, but their practical performance is limited by sluggish interfacial kinetics and severe shuttle of soluble intermediates. Here we report a core-shell $Co_2P_2O_7$@CoP catalytic electrode that addresses these two challenges through an integrated conductivity-adsorption strategy. In this architecture, the CoP shell serves as a highly conductive pathway for rapid charge transfer, while the $Co_2P_2O_7$ core provides polar P-O sites that strongly immobilize both polysulfide and polyiodide intermediates. This dual-function design enables simultaneous acceleration of the S^{2-}/S_x^{2-} and I^-/I^{3-} redox reactions and effective suppression of side reactions. As a result, the assembled SIFB delivers an initial energy efficiency of 84.53% at 20 mA·cm^{-2} and maintains 64.61% after 50 cycles. Long-term operation at 10 mA·cm^{-2} and 10% SOC remains stable for 400 cycles with energy efficiency above 70%. Density functional theory (DFT) calculations reveal that interfacial electronic coupling, rather than simple phase addition, is responsible for the enhanced adsorption and reduced reaction barriers.

KEYWORDS

polysulfide/iodide redox flow batteries, heterostructured electrocatalyst, dual-function design, high-efficiency

1 Introduction

Polysulfide/iodide redox flow batteries (SIFBs) are regarded as one of the most promising large-scale energy-storage technologies because of their high theoretical energy density, low cost, abundant active species, and intrinsic safety of aqueous systems [1–3]. In particular, the I^-/I_3^- and S^{2-}/S_x^{2-} redox couples exhibit high solubility in aqueous electrolytes, which makes SIFBs especially attractive for medium- and long-duration energy storage [4, 5]. However, practical application of SIFBs remains constrained by two major challenges. First, both the I^-/I_3^- and S^{2-}/S_x^{2-} couples involve multistep electron-transfer processes at the electrode/electrolyte interface, leading to sluggish kinetics, large charge-transfer resistance, and severe voltage polarization, thereby lowering energy efficiency and power output [6, 7]. Second, the soluble polyiodide and polysulfide intermediates generated during cycling, especially long-chain polysulfides, are prone to migration and shuttle, resulting in active-material loss, deactivation of surface active sites, and degraded cycling stability [8–10]. Therefore, developing efficient catalytic electrodes that can simultaneously accelerate the I^-/I_3^- and S^{2-}/S_x^{2-} redox reactions while effectively anchoring soluble intermediates is central to advancing SIFBs toward high performance and practical deployment.

In recent years, research on SIFB electrocatalysts has focused extensively on transition-metal-based materials, especially metal sulfides, oxides, and phosphides, because their local electronic structures can strongly regulate intermediate adsorption and interfacial redox kinetics [11, 12]. Among them, cobalt phosphides are considered highly promising candidates owing to their high electrical conductivity and favorable electrocatalytic activity. Phosphides represented by CoP can promote interfacial electron transfer and accelerate redox reactions [13, 14]; however, their surface polarity is relatively limited, and their chemical affinity toward soluble sulfur- and iodine-containing intermediates remains insufficient. In contrast, cobalt phosphates or phosphorus-oxygen coordinated phases with polar P-O environments often interact more strongly with polysulfides and polyiodides, thereby

Address correspondence to Xiaoyang Cheng, xycheng@xmu.edu.cn; Jia He, hejia1225@126.com; Xijun Liu, xjliu@gxu.edu.cn

more effectively suppressing the shuttle effect [15, 16], but their poor electrical conductivity is unfavorable for rapid charge transfer. This intrinsic trade-off between conductivity and polar adsorption capability indicates that a single-component material is usually unable to meet the dual requirements of fast reaction kinetics and high cycling stability in SIFBs [17]. By comparison, constructing a core-shell heterostructure composed of a conductive phosphide phase and a polar phosphorus-oxygen phase may enable synergistic optimization of electron transport, active-species adsorption, and reaction-pathway regulation at the same interface, thereby improving both the thermodynamics and kinetics of electrode reactions [18–23].

Based on this design concept, we constructed a $Co_2P_2O_7$@CoP core-shell electrode. In this architecture, the conductive CoP shell promotes rapid charge transfer, while the $Co_2P_2O_7$ core provides polar P-O sites for strong adsorption of polysulfide and polyiodide intermediates. The assembled symmetric SIFB delivers an initial energy efficiency of 84.53% at 20 mA·cm^{-2} and retains 64.61% after 50 cycles. During long-term operation at 10 mA·cm^{-2} and 10% SOC, the battery maintains energy efficiency above 70% after 400 cycles, with capacity retention above 90%. After electrolyte refreshing, the energy efficiency quickly recovers to 84.25%, indicating that the performance decay mainly originates from electrolyte-side parasitic reactions rather than intrinsic electrode deactivation. Density functional theory calculations further reveal that the enhanced performance arises from electronic coupling at the $Co_2P_2O_7$/CoP heterointerface, which strengthens the adsorption of iodine-containing and long-chain polysulfide intermediates and lowers the barriers of key sulfur-conversion steps. These results highlight core-shell heterostructure engineering as an effective strategy for developing high-performance sulfur-iodine flow batteries.

2 Results and discussion

2.1 Synthesis and structural characterizations

The rational design of $Co_2P_2O_7$@CoP core-shell heterostructures was achieved through a two-step synthesis protocol (Fig. 1(a)): (i) hydrothermal growth of a Co_3O_4 precursor on graphite felt (GF), followed by (ii) high-temperature phosphidation at 900 °C using NaH_2PO_2 as the phosphorus source. During phosphidation, PH_3 generated in situ from NaH_2PO_2 decomposition preferentially reacts with the outer surface of Co_3O_4, forming a crystalline CoP shell, while the inner region undergoes partial phosphidation to form a weakly crystalline $Co_2P_2O_7$ core due to diffusion limitations. This surface-initiated conversion is fundamentally different from simple physical mixing and enables intimate interfacial engineering within the core-shell architecture [24, 25]. The phase evolution was first confirmed by XRD (Fig. 1(b)). The

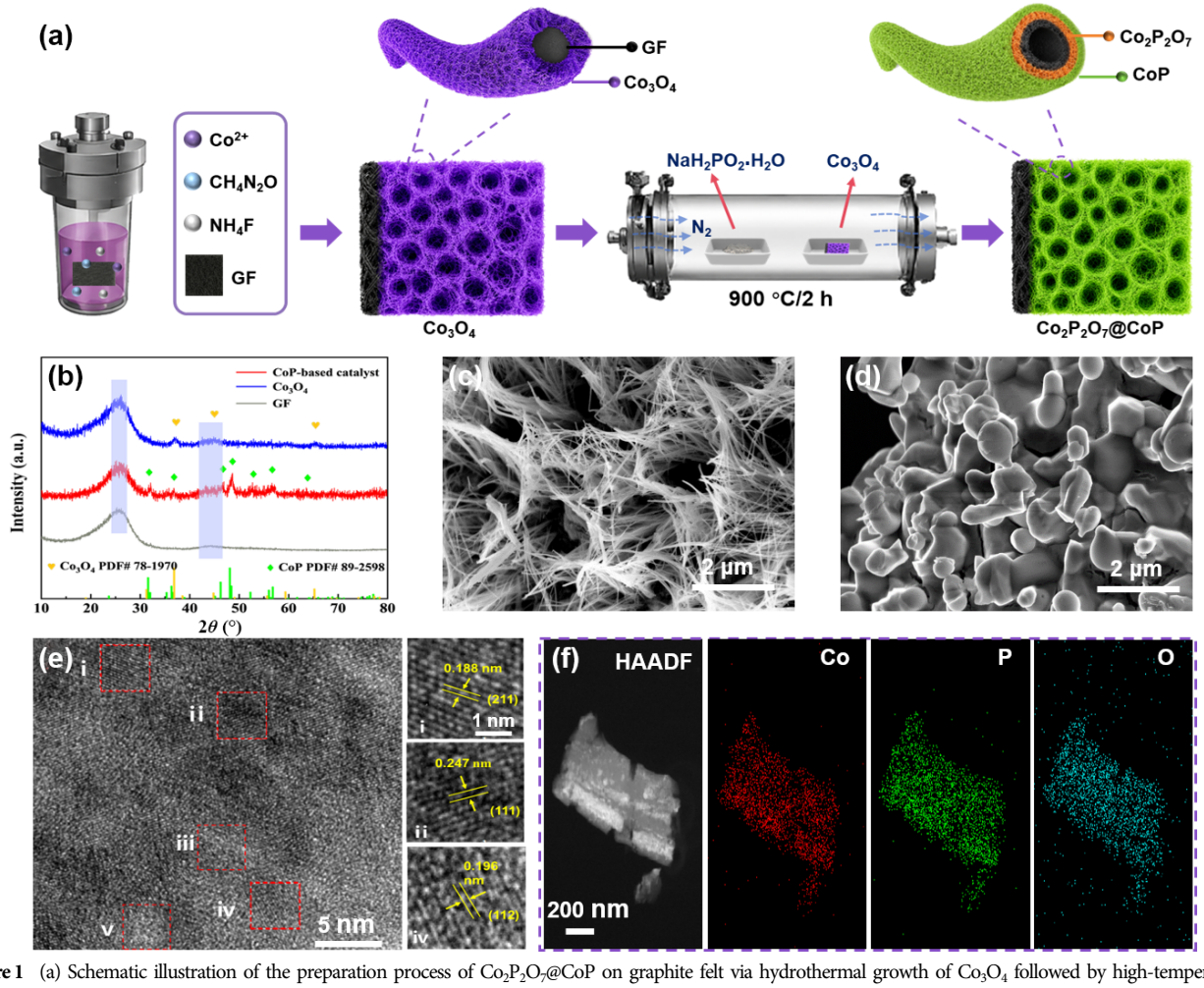

Figure 1 (a) Schematic illustration of the preparation process of $Co_2P_2O_7$@CoP on graphite felt via hydrothermal growth of Co_3O_4 followed by high-temperature phosphidation using $NaH_2PO_2·H_2O$. (b) XRD patterns of GF, Co_3O_4 precursor, and CoP-based catalyst. (c, d) SEM images of the Co_3O_4 precursor and $Co_2P_2O_7$@CoP catalyst, respectively. (e) HRTEM image of $Co_2P_2O_7$@CoP and the corresponding enlarged lattice-fringe images from selected region. (f) HAADF-STEM image and corresponding EDS elemental mappings of Co, P, and O in $Co_2P_2O_7$@CoP.

precursor exhibits characteristic diffraction peaks of Co_3O_4 (PDF#78-1970), whereas the phosphidated product shows sharp peaks mainly indexed to CoP (PDF#89-2598), with no obvious residual Co_3O_4 signals, indicating effective phase transformation and high crystallinity of the CoP phase. The absence of broad amorphous humps further suggests the formation of a crystalline outer shell [26]. SEM images show that the Co_3O_4 precursor consists of interwoven slender nanowires with a loose porous network structure (Fig. 1(c) and Fig. S1(a) in the Electronic Supplementary Material (ESM)); after phosphidation, $Co_2P_2O_7$@CoP transforms into a compact structure assembled from particle-like or short rod-like units (Fig. 1(d) and Fig. S1(b) in the ESM), indicating significant phase transformation and morphological reconstruction during the phosphidation process [27].

The core-shell feature is further supported by high-resolution TEM characterization. As shown in Fig. 1(e), the HRTEM image reveals a distinct contrast gradient from the particle surface to the interior. The outermost high-contrast region (region ii) exhibits clear lattice fringes with a spacing of 0.247 nm, corresponding to the CoP (111) plane, confirming the formation of a crystalline CoP shell. The inner shell regions (regions i and iv) show well-resolved lattice spacings of 0.188 and 0.196 nm, which can be assigned to the CoP (211) and CoP (112) planes, respectively, indicating the presence of an inner CoP-rich layer. In contrast, the central low-contrast regions (regions iii and v) display lower contrast and discontinuous lattice fringes, characteristic of a weakly crystalline $Co_2P_2O_7$ core. This spatially resolved contrast variation provides direct evidence for the $Co_2P_2O_7$@CoP core-shell topology and is consistent with the proposed surface-initiated phosphidation mechanism. High-angle annular dark-field scanning transmission electron microscopy (HAADF-STEM) and energy dispersive spectroscopy (EDS) elemental mapping further reveal the uniform distribution of Co, P, and O throughout the particle (Fig. 1(f)), confirming the coexistence of Co-P and P-O species. Quantitative EDS analysis gives atomic fractions of 14.19% Co, 23.76% P, and 62.06% O (Table S1 in the ESM), corresponding to a Co:P:O ratio of approximately 1:1.68:4.37. The high oxygen content verifies the presence of abundant P-O bonds [28], while the P/Co ratio higher than unity suggests the coexistence of a phosphorus-rich $Co_2P_2O_7$ phase with a minor Co-P phosphide phase, further supporting an internal $Co_2P_2O_7$-rich core and a surface CoP-rich shell.

To further confirm the surface chemical states of the $Co_2P_2O_7$@CoP, X-ray photoelectron spectroscopy (XPS) was performed. The survey spectrum shows the presence of Co, P, O, and C elements (Fig. S2 in the ESM), consistent with the EDS results. The C signal mainly originates from the graphite felt substrate [29], while Co, P, and O are associated with the phosphidated Co-based active species. The high-resolution Co 2p spectrum exhibits typical Co^{2+}/Co^{3+} mixed-valence features accompanied by satellite peaks (Fig. 2(a)). The peak at 781.4 eV is assigned to Co^{3+} species mainly related to the CoP shell, whereas the peak at 797.5 eV corresponds to Co^{2+} species associated with the $Co_2P_2O_7$ core [30, 31], indicating the coexistence of different Co coordination environments in the core-shell structure.

The P 2p spectrum can be deconvoluted into two groups of peaks (Fig. 2(b)). The peaks at 133.5 and 131.5 eV correspond to P^{3-} species from Co-P bonds in CoP, while the peaks at 135.5 and 137.0 eV are attributed to P^{5+} species from P-O bonds in $Co_2P_2O_7$ [15, 32]. The simultaneous presence of P^{3-} and P^{5+} confirms the coexistence of cobalt phosphide and cobalt pyrophosphate phases. In the O 1s spectrum, the peak at 531.5 eV is assigned to P-O bonds in $Co_2P_2O_7$, and the peak at 533.1 eV is related to surface-

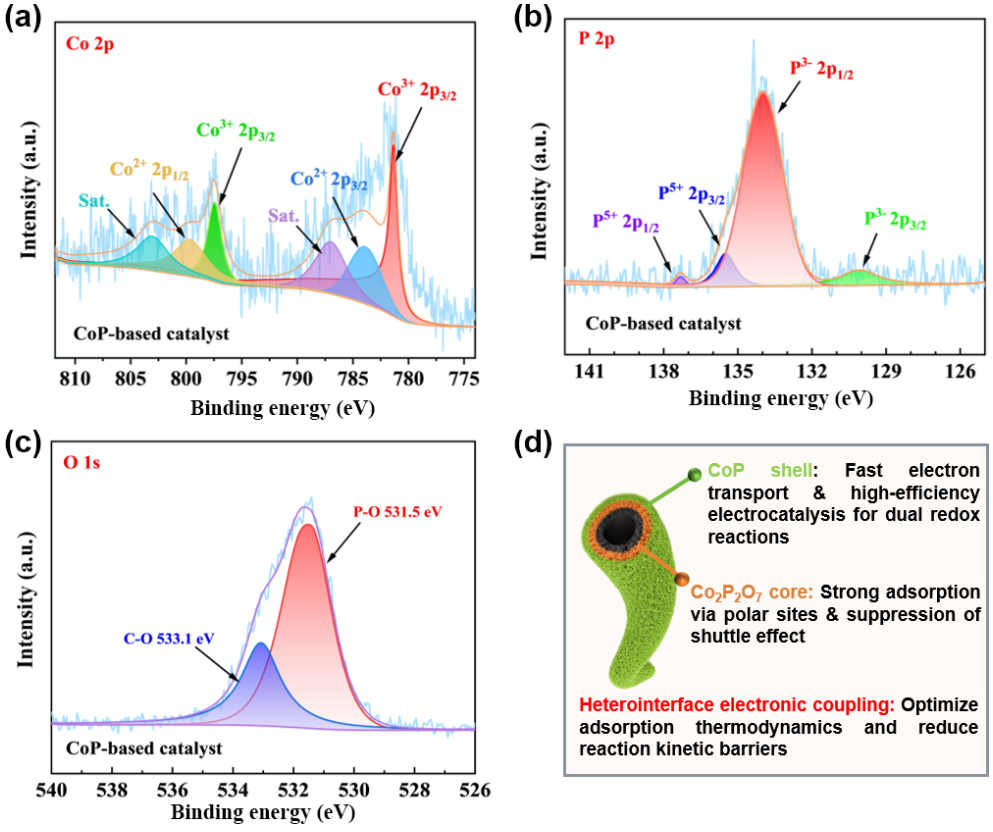

Figure 2 (a) Co 2p, (b) P 2p and (c) O 1s XPS spectra of $Co_2P_2O_7$@CoP. (d) Schematic illustration of the $Co_2P_2O_7$@CoP core-shell heterostructure, in which the CoP shell provides conductive pathways for charge transfer and the $Co_2P_2O_7$ core supplies polar P-O sites for intermediate adsorption.

adsorbed H_2O/-OH species (Fig. 2(c)), which may improve electrolyte wettability and ion transport at the electrode interface [33]. XPS quantitative analysis shows that the atomic percentages of C, Co, P, and O are 75.53%, 3.00%, 3.74%, and 17.83% (Table S2 in the ESM), respectively. The P/Co atomic ratio slightly higher than unity, together with the considerable O content, further indicates the existence of phosphate species in the phosphidated product. Therefore, the XPS results are consistent with the XRD, TEM, and EDS analyses, further confirming that the obtained electrode possesses a $Co_2P_2O_7$@CoP core-shell heterostructure (Fig. 2(d)) rather than a simple physical mixture of $Co_2P_2O_7$ and CoP phases [34].

2.2 Adsorption and electrocatalytic activity

The performance of SIFBs is mainly limited by the shuttle effect arising from the crossover of soluble S_x^{2-}/I_3^- intermediates and by the sluggish reaction kinetics of the S^{2-}/S_x^{2-} and I^-/I_3^- redox couples [35, 36]. Therefore, constructing a $Co_2P_2O_7$@CoP core-shell heterostructure with both intermediate-capturing capability and charge-transfer-promoting functionality is expected to simultaneously suppress the shuttle effect and accelerate redox conversion. First, visual adsorption experiments and UV-vis spectroscopy were conducted to compare the adsorption behavior of GF, Co_3O_4, and $Co_2P_2O_7$@CoP electrodes toward I_3^- and S_x^{2-} active species. As shown in Figs. 3(a) and 3(b), after standing for 12 h, the colors of the I^-/I_3^- and S^{2-}/S_x^{2-} electrolytes treated with GF showed almost no change, indicating the weak adsorption capability of GF toward iodine/sulfur intermediates. The solutions treated with Co_3O_4 became noticeably lighter in color, suggesting moderate adsorption capability. In contrast, both solutions treated with $Co_2P_2O_7$@CoP became nearly colorless, demonstrating its strongest active-species-capturing ability. Moreover, the

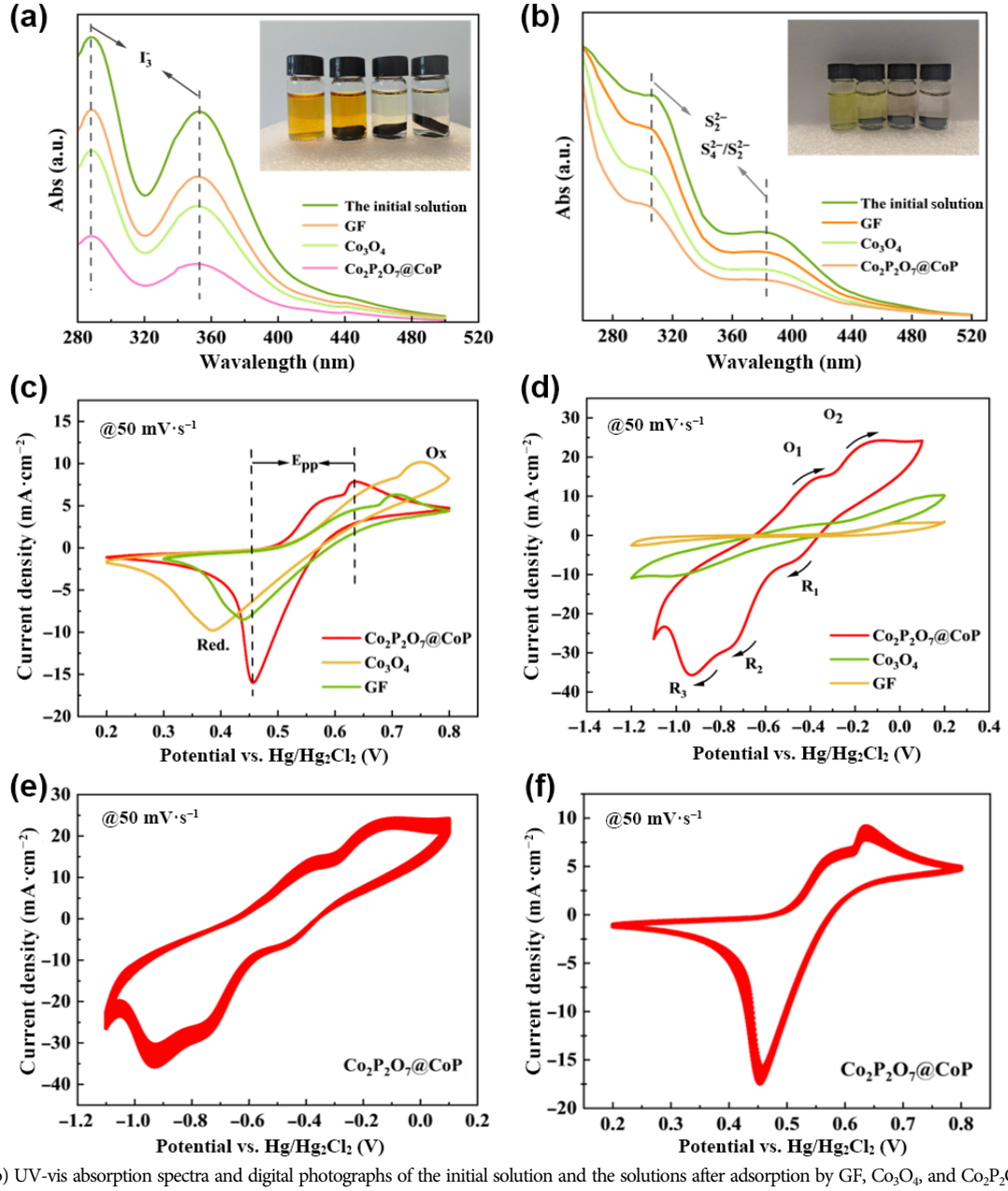

Figure 3 (a, b) UV-vis absorption spectra and digital photographs of the initial solution and the solutions after adsorption by GF, Co_3O_4, and $Co_2P_2O_7$@CoP for I_3^- and S_x^{2-} species, respectively. (c, d) CV curves of GF, Co_3O_4, and $Co_2P_2O_7$@CoP electrodes in 0.1 M NaI_3 + 0.5 M NaCl solution and 0.06 M Na_2S + 0.02 M S + 0.5 M NaCl solution, respectively, at 50 mV·s^{-1}. (e, f) CV cycling stability of $Co_2P_2O_7$@CoP in 0.06 M Na_2S + 0.02 M S + 0.5 M NaCl and 0.1 M NaI_3 + 0.5 M NaCl solution, respectively, at 50 mV·s^{-1} for 200 cycles.

adsorption and permeability phenomena of I_3^- and S_x^{2-} are intuitively observed in the H-type cells with static diffusion tests (Fig. S3 in the ESM), respectively. As depicted, the chamber with water shows a negligible colour change separated by $Co_2P_2O_7$@CoP. UV-vis spectra further confirmed that the characteristic absorption peaks of I_3^- at 290 and 352 nm (Fig. 3(a)) and those of S_x^{2-} at 260, 310, and 370 nm (Fig. 3(b)) were significantly decreased [37, 38], indicating the stronger adsorption interaction of $Co_2P_2O_7$@CoP with both types of redox intermediates. This adsorption advantage is beneficial for restricting the crossover of soluble I_3^- and S_x^{2-}, thereby alleviating the shuttle effect and improving subsequent interfacial reaction efficiency [5]. Besides, the electrochemical active surface area via double-layer capacitance (C_{dl}) has been recorded according to the cyclic voltammetry measurements. As shown, $Co_2P_2O_7$@CoP presents C_{dl} values of 10.9 and 0.11 mF·cm^{-2} in Na_2S and NaI_3, respectively, both of them are greater than those of the two references (Figs. S4 and S5 in the ESM), further confirming the superiority of the designed core-shell structure.

Subsequently, cyclic voltammetry (CV) was performed to evaluate the electrocatalytic activity of $Co_2P_2O_7$@CoP toward the S^{2-}/S_x^{2-} and I^-/I_3^- redox reactions. As shown in Fig. 3(c), in the I^-/I_3^- electrolyte, all three electrodes showed obvious redox peaks; however, $Co_2P_2O_7$@CoP exhibited the smallest E_{pp} of 0.18 V, much lower than those of GF (0.36 V) and Co_3O_4 (0.27 V) (Table S3 in the ESM). Moreover, the $|J_{Red}/J_{ox}|$ value of $Co_2P_2O_7$@CoP reached 2.03, higher than those of GF (0.96) and Co_3O_4 (1.35), indicating its higher reaction reversibility and faster electron-transfer kinetics for the I^-/I_3^- redox couple [37]. As shown in Fig. 3(d), in the S^{2-}/S_x^{2-} electrolyte, GF and Co_3O_4 mainly exhibited one pair of redox peaks, whereas $Co_2P_2O_7$@CoP displayed two oxidation peaks and three reduction peaks, indicating that polysulfides underwent a more complete multistep electron-transfer process on its surface [39]. Meanwhile, $Co_2P_2O_7$@CoP showed a smaller peak potential separation (E_{pp} = 0.24 V) than Co_3O_4 (0.29 V) and GF (0.32 V), suggesting that it effectively reduces reaction polarization and improves redox reversibility [40]. In addition, the pure $Co_2P_2O_7$ electrode has been prepared and the results demonstrated an inferior activity for S^{2-}/S_x^{2-} and I^-/I_3^- conversion (Figs. S6 and S7 in the ESM).

To further analyze mass-transfer behavior, CV tests were conducted over a scan-rate range of 10–100 mV·s^{-1} (Fig. S8 in the ESM). As the scan rate increased, the oxidation/reduction peak currents of all electrodes gradually increased, accompanied by enlarged peak separations, suggesting that the electrode processes at high scan rates were jointly affected by diffusion limitation and polarization. The peak currents showed good linear relationships with the square root of the scan rate ($v^{1/2}$) (Fig. S9 in the ESM), indicating that the S^{2-}/S_x^{2-} reaction was mainly diffusion-controlled. Compared with Co_3O_4, $Co_2P_2O_7$@CoP exhibited a larger fitted slope, suggesting a higher diffusion coefficient of active species and faster interfacial mass-transfer rate [41, 42]. These results demonstrate that the core-shell heterostructure not only enhances intermediate adsorption but also promotes the rapid transport of active species from the electrolyte to the electrode surface, thereby accelerating the overall redox reactions. Finally, the electrode stability was further verified by continuous CV cycling for 200 cycles.

As shown in Figs. 3(e) and 3(f), in both the S^{2-}/S_x^{2-} and I^-/I_3^- electrolytes, the CV curves of $Co_2P_2O_7$@CoP almost overlapped before and after cycling, with no obvious attenuation in redox peak positions or peak currents, indicating its excellent electrochemical reversibility and structural stability. This stability mainly originates from the core-shell heterostructure of $Co_2P_2O_7$@CoP: the CoP shell facilitates electron transport and interfacial catalysis, while the $Co_2P_2O_7$ core provides a stable phosphorus–oxygen coordination environment. Their synergy enhances the stability of active sites and suppresses structural degradation. Therefore, $Co_2P_2O_7$@CoP can maintain stable catalytic activity during continuous redox processes, providing an important foundation for the high-efficiency and long-life operation of SIFBs.

2.3 Density functional theory (DFT) calculations

To elucidate the origin of the bifunctional catalytic activity of the $Co_2P_2O_7$@CoP core-shell heterostructure, $Co_2P_2O_7$ and $Co_2P_2O_7$@CoP models were constructed and investigated by DFT calculations. As shown in Figs. 4(a) and 4(b), the density of states (DOS) results show that $Co_2P_2O_7$@CoP exhibits a higher DOS near the Fermi level than pristine $Co_2P_2O_7$, indicating improved electronic conductivity and faster charge transfer between the electrode and reaction intermediates. This result suggests that electronic structure reconstruction occurs at the $Co_2P_2O_7$/CoP interface, providing favorable conditions for the rapid redox reactions of I^-/I_3^- and S^{2-}/S_x^{2-} couples. Adsorption energy calculations further reveal the thermodynamic basis for shuttle suppression by $Co_2P_2O_7$@CoP.

As shown in Fig. 4(c), the optimized adsorption configurations of key iodine- and sulfur-containing intermediates on $Co_2P_2O_7$@CoP intuitively reveal the stepwise evolution of the I^-/I_3^- and S^{2-}/S_x^{2-} redox processes. As shown in Table S4 in the ESM, pristine $Co_2P_2O_7$ shows weak adsorption toward polysulfides, especially with positive adsorption energies for Na_2S_4 and Na_2S_8 (+0.7719 and +0.9432 eV, respectively), indicating that long-chain polysulfide species tend to desorb from the electrode surface and migrate into the electrolyte, making shuttle suppression difficult [43]. Meanwhile, the adsorption energies of I_2 and I_3^- on pristine $Co_2P_2O_7$ are –1.48 and –1.115 eV, respectively, suggesting limited anchoring ability toward iodine intermediates [44]. In contrast, $Co_2P_2O_7$@CoP exhibits significantly enhanced adsorption toward both polysulfide and iodine species, with adsorption energies of –4.81, –4.54, and –3.98 eV for Na_2S_8, Na_2S_6, and Na_2S_4, respectively, and –1.90 and –2.08 eV for I_2 and I_3^-, respectively. These results demonstrate that $Co_2P_2O_7$@CoP can effectively anchor soluble polysulfide and iodine species, reduce their migration tendency in the electrolyte, and suppress the shuttle effect at the source [45]. Free energy calculations further demonstrate the kinetic advantages of $Co_2P_2O_7$@CoP.

As shown in Figs. 4(d) and 4(e), for the I^-/I_3^- conversion pathway, the potential-determining step (PDS) on pristine $Co_2P_2O_7$ is $*I^- \rightarrow *I_2$, with a free-energy change of –0.32 eV. In contrast, the PDS on $Co_2P_2O_7$@CoP shifts to $* \rightarrow *I^-$, with a much lower free-energy change of only –1.84 eV, indicating that the core-shell structure significantly lowers the reaction barrier for iodine species conversion. For the S^{2-}/S_x^{2-} conversion process, the PDS free-energy change of the $* \rightarrow *S^{2-}$ step on $Co_2P_2O_7$@CoP is –4.1 eV, much lower than that on pristine $Co_2P_2O_7$ (–2.4 eV), indicating stronger polysulfide anchoring and more favorable sulfur-species conversion. Meanwhile, the energy barrier for the $*S_4^{2-} \rightarrow *S_6^{2-}$ step is only 0.35 eV, lower than that on pristine $Co_2P_2O_7$ (0.41 eV), suggesting promoted stepwise conversion of polysulfide species. These results demonstrate that, compared with pristine $Co_2P_2O_7$, $Co_2P_2O_7$@CoP achieves stronger adsorption of iodine/polysulfide species and lower barriers for key conversion

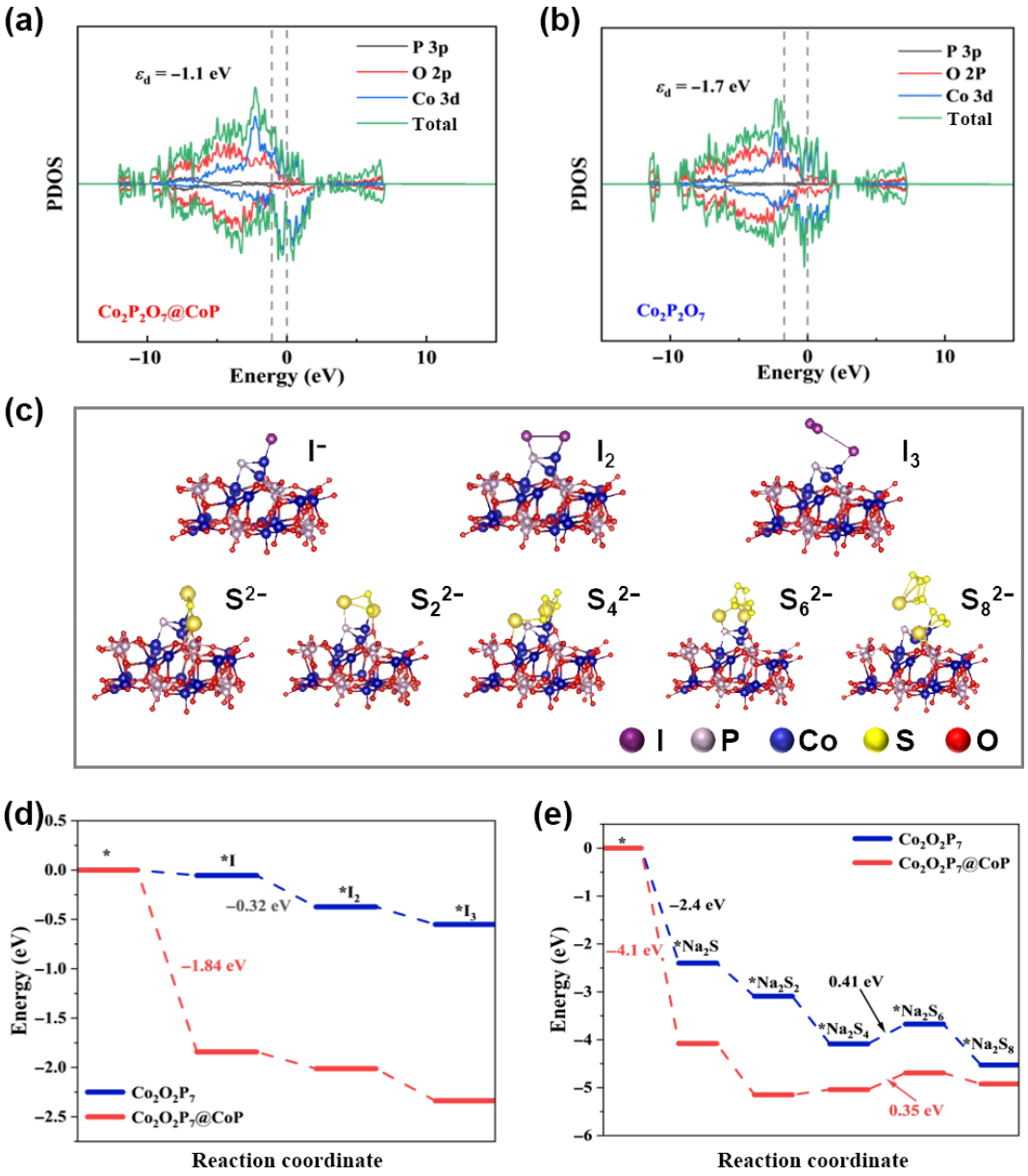

Figure 4 Calculated PDOS of (a) $Co_2P_2O_7$@CoP and (b) $Co_2P_2O_7$, with aligned Fermi level. (c) Optimized adsorption configurations of I-containing and S-containing intermediates on $Co_2P_2O_7$@CoP. (d, e) Free-energy diagrams of I^-/I_3^- and S^{2-}/S_x^{2-} conversion reactions on $Co_2P_2O_7$@CoP and $Co_2P_2O_7$.

steps. Therefore, the superior performance of $Co_2P_2O_7$@CoP mainly originates from the synergistic electronic coupling at the $Co_2P_2O_7$/CoP interface, which enhances reactant anchoring, accelerates redox kinetics at both electrodes, lowers electrochemical polarization, and provides a theoretical basis for its excellent bifunctional catalytic activity and redox flow battery performance [45–47].

2.4 Redox flow battery performance

To evaluate the practical applicability of the $Co_2P_2O_7$@CoP core-shell electrode in SIFBs, a symmetric cell was assembled using $Co_2P_2O_7$@CoP as both the positive and negative electrodes. As illustrated in Fig. 5(a), the I^-/I_3^- and S^{2-}/S_x^{2-} couples serve as the positive and negative redox couples, respectively, and Na^+ migrates through the membrane during cycling to maintain charge balance. At a current density of 20 mA·cm^{-2}, the $Co_2P_2O_7$@CoP-based cell exhibits a significantly reduced charge–discharge voltage gap of only 212 mV, much smaller than those of Co_3O_4 (457 mV) and bare GF (648 mV) (Fig. 5(b)). The narrowed voltage polarization indicates that the $Co_2P_2O_7$@CoP electrode effectively lowers the reaction overpotential and accelerates the interfacial kinetics of both the I^-/I_3^- and S^{2-}/S_x^{2-} redox couples. The lower charging plateau and higher discharging plateau further confirm improved reaction reversibility and reduced energy loss [48].

Rate performance tests show that $Co_2P_2O_7$@CoP delivers higher voltage efficiency (VE) and energy efficiency (EE) over the entire tested current range of 20–100 mA·cm^{-2} (Fig. 5(c)), indicating lower charge-transfer resistance and faster interfacial redox kinetics [49]. At 20, 40, and 60 mA·cm^{-2}, both $Co_2P_2O_7$@CoP and Co_3O_4 maintain nearly 100% Coulombic efficiency (CE). When the current density increases to 80 and 100 mA·cm^{-2}, CE decreases for both electrodes; however, $Co_2P_2O_7$@CoP still retains a slightly higher CE than Co_3O_4, whereas GF shows the most pronounced decay. This result suggests that $Co_2P_2O_7$@CoP has better high-rate tolerance and stronger capability to suppress side reactions [5]. The galvanostatic charge-discharge profiles of $Co_2P_2O_7$@CoP at

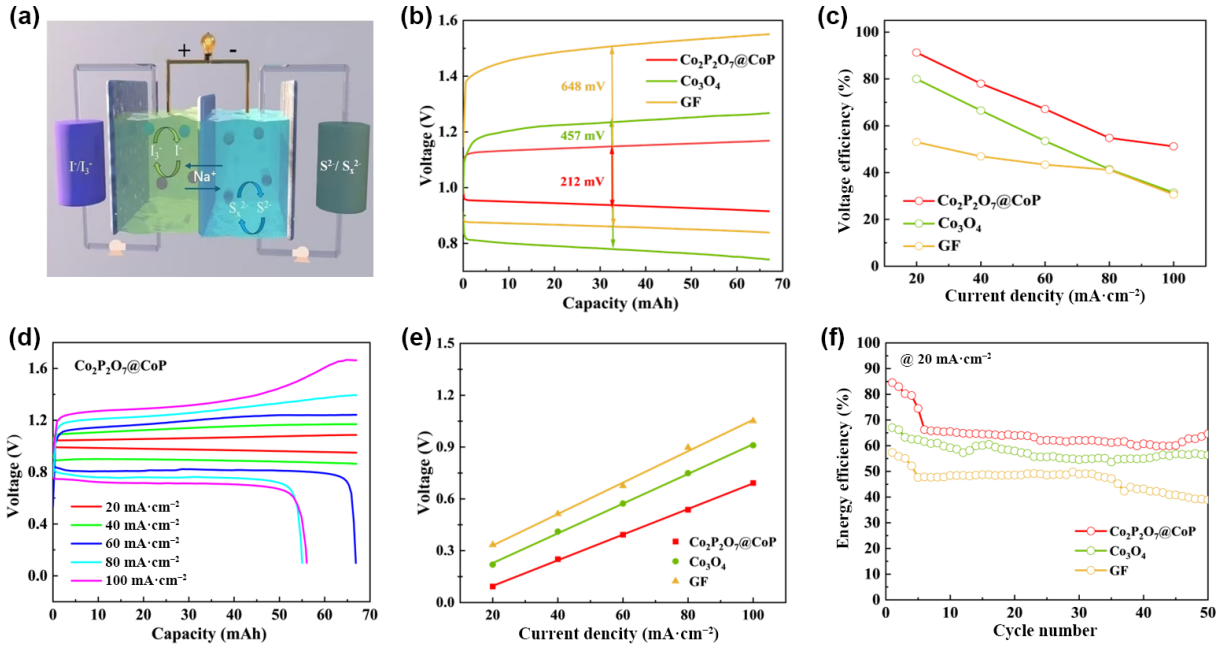

Figure 5 (a) Schematic illustration of the polysulfide/iodide redox flow battery. (b) Voltage polarization curves of different electrodes at 20 mA·cm^{-2}: discharge to 50% and charge to 100%. (c) Voltage efficiency at different current densities. (d) Charge-discharge profiles of $Co_2P_2O_7$@CoP from 20 to 100 mA·cm^{-2}. (e) Average voltage gap as a function of current density. (f) Cycling energy efficiency at 20 mA·cm^{-2} for 50 cycles.

different current densities further show stable charge-discharge behavior and small voltage hysteresis (Fig. 5(d)). The slope of the average voltage gap-current density plot reflects the overall cell resistance (Fig. 5(e)). $Co_2P_2O_7$@CoP shows the lowest slope, corresponding to only 54% and 28% of those of Co_3O_4 and GF, respectively, further demonstrating that the core-shell heterostructure effectively reduces ohmic loss and activation polarization. In addition, its smallest intercept indicates the lowest intrinsic polarization at low current densities [50].

Cycling stability was evaluated at 20 mA·cm^{-2} and 50% state of charge (SOC) (Fig. 5(f)). The $Co_2P_2O_7$@CoP cell delivers an initial EE of 84.53%, substantially higher than those of Co_3O_4 (67.00%) and GF (57.73%). After 50 cycles, $Co_2P_2O_7$@CoP still maintains an EE of 64.61%, corresponding to a retention of 76.43%, whereas Co_3O_4 and GF decrease to 56.40% and 38.91%, respectively. The CE of $Co_2P_2O_7$@CoP remains above 95% throughout cycling and reaches 97.2% after 50 cycles (Fig. S10 in the ESM), indicating effective suppression of active-species loss and shuttle effects. In contrast, the VE decreases from approximately 82% to 66.59%, suggesting that the EE decay mainly originates from the gradual increase in voltage polarization rather than severe irreversible capacity loss [51]. Post-cycling electrode photographs further support this conclusion: only slight residual deposits are observed on $Co_2P_2O_7$@CoP, whereas obvious iodine-related precipitates appear on GF and Co_3O_4 (Fig. S11 in the ESM). This result indicates that the polar P-O sites in $Co_2P_2O_7$ can effectively anchor soluble intermediates and preserve more exposed catalytic surfaces.

Long-term cycling performance was further tested at 10 mA·cm^{-2} and 10% SOC. The $Co_2P_2O_7$@CoP cell achieves an initial EE of 87% and retains approximately 75% after 200 cycles (Fig. S12(a) in the ESM). After replacing the electrolyte at the 200th cycle, the EE rapidly recovers to 84.25% and remains above 70% after extended cycling to 400 cycles. In contrast, the EE values of Co_3O_4 and GF decrease to approximately 43% and 40% after 200 cycles, respectively. The recovery of efficiency after electrolyte refreshment indicates that the performance decay mainly arises from electrolyte-side parasitic reactions, by-product accumulation, or ion concentration imbalance, rather than structural degradation of the $Co_2P_2O_7$@CoP electrode. Capacity retention results are consistent with the above analysis. $Co_2P_2O_7$@CoP maintains a capacity retention above 90% over 400 cycles (Fig. S12(b) in the ESM), significantly outperforming the control electrodes. Galvanostatic charge-discharge profiles show that $Co_2P_2O_7$@CoP has a lower charging voltage, a higher discharging voltage, and a smaller voltage gap (Fig. S12(c) in the ESM). Its maximum discharge capacity reaches approximately 115 mAh, higher than those of Co_3O_4 (~95 mAh) and GF (~98 mAh), demonstrating improved utilization of active species. In addition, the developed $Co_2P_2O_7$@CoP delivers a competitive advantage in terms of energy efficiency and cycling durability as compared with other reported bifunctional electrocatalysts (see Table S5 in the ESM for details). The morphology characterizations manifested the robust structural feature of $Co_2P_2O_7$@CoP during the long-term cycling test (Fig. S13 in the ESM). Overall, the $Co_2P_2O_7$@CoP core-shell electrode integrates thermodynamic adsorption from the polar P-O sites in the $Co_2P_2O_7$ core with kinetic charge-transfer promotion from the conductive CoP shell [52]. This synergy accelerates the reversible conversion of I^-/I_3^- and S^{2-}/S_x^{2-} while mitigating shuttle effects and active-species deposition. As a result, $Co_2P_2O_7$@CoP achieves simultaneous improvement in low polarization, high EE/CE, and long-term cycling stability, providing an effective strategy for designing high-performance SIFB electrodes.

3 Conclusions

In summary, our findings clarify the key structural requirements for phosphide-based electrodes in sulfur-iodine flow batteries. We demonstrate that the performance improvement of such electrodes is not governed solely by increasing phosphidation degree or conductivity, but rather by balancing charge transport, polar active sites, and interfacial regulation. By employing a controllable phosphidation strategy, we achieve the coordinated

construction of a $Co_2P_2O_7$@CoP core-shell heterostructure, enabling the integration of fast electron-transfer pathways with effective adsorption and conversion of soluble polysulfide/polyiodide intermediates. In this architecture, the CoP shell accelerates charge transfer and redox kinetics, while the $Co_2P_2O_7$ core provides polar P-O coordination environments and defect-related active sites for intermediate anchoring and catalytic conversion. More importantly, the heterointerface induces electronic structure modulation, which optimizes intermediate adsorption and lowers the energy barrier of the interfacial redox process. This design allows the simultaneous enhancement of reaction kinetics and suppression of shuttle behavior. These findings not only demonstrate the effectiveness of controllable phosphidation in constructing heterostructured SIFB electrodes, but also provide a general framework for coordinating conductivity, intermediate anchoring, and interfacial catalytic activity in flow-battery systems.

4 Method

4.1 Experimental

Synthesis of Co_3O_4. Co_3O_4 grown on graphite felt (GF) was synthesized by a hydrothermal method followed by thermal annealing. Typically, graphite felt (GF, 2 cm × 4 cm) was first immersed in 6 M H_2SO_4 for 12 h, then thoroughly washed with deionized water until the washing solution became nearly neutral. The treated GF was subsequently annealed at 300 °C for 2 h under an Ar atmosphere. In a typical synthesis, 1.080 g NH_4F, 1.2012 g CH_4N_2O, and 1.1640 g $Co(NO_3)_2{\cdot}6H_2O$ were dissolved in 75 mL deionized water under stirring to form a homogeneous pink solution. The pretreated GF was immersed in the solution, and the mixture was transferred into a 100 mL Teflon-lined stainless-steel autoclave. The autoclave was heated at 140 °C for 12 h. After cooling to room temperature, the GF covered with pink precursor was taken out, rinsed thoroughly with deionized water and ultrasonicated to remove loosely attached particles. The obtained sample was dried at 60 °C for 24 h and then annealed at 400 °C for 2 h under vacuum to obtain Co_3O_4 grown on GF, denoted as Co_3O_4.

Synthesis of $Co_2P_2O_7$@CoP. The $Co_2P_2O_7$@CoP catalyst was prepared by phosphidation of the as-synthesized Co_3O_4 precursor using $NaH_2PO_2{\cdot}H_2O$ as the phosphorus source. Typically, 1.27 g of $NaH_2PO_2{\cdot}H_2O$ and the Co_3O_4 precursor were placed at the upstream and downstream positions of a tube furnace, respectively. The phosphidation process was carried out at 900 °C for 2 h under a flowing N_2 atmosphere, followed by natural cooling to room temperature. The resulting self-supported electrode was collected and denoted as the $Co_2P_2O_7$@CoP catalyst.

4.2 Electrochemical measurements

CV measurements were performed on a CHI760D electrochemical workstation with a typical three-electrode system, where a platinum sheet, a saturated calomel electrode (Hg/Hg_2Cl_2), and the as-prepared catalyst or graphite felt (GF) were used as the counter, reference, and working electrodes, respectively. For the preparation of the working electrode, 10 mg of powder catalyst was dispersed in a mixture of 500 μL deionized water and 500 μL isopropyl alcohol, followed by the addition of 20 μL of 5 wt.% Nafion solution, and the mixture was ultrasonicated for 30 min to form a homogeneous ink, which was then uniformly drop-cast onto a 3 mm-diameter glassy carbon electrode and dried at room temperature, while bare GF was directly tested as a control working electrode. CV tests were carried out in 0.06 M Na_2S + 0.02 M S + 0.5 M NaCl and 0.1 M NaI_3 + 0.5 M NaCl aqueous solutions at a fixed scan rate of 50 $mV{\cdot}s^{-1}$ or a series of gradient scan rates from 10 to 100 $mV{\cdot}s^{-1}$ (10, 20, 30, 40, 50, 60, 70, 80, 90, 100 $mV{\cdot}s^{-1}$). The separator used in this work is Nafion N117 membrane (Suzhou Shengnuo Technology Co., Ltd.). The membrane thickness is 183 μm (7.2 mil), with an ion exchange capacity (IEC) of 0.89–0.90 $meq{\cdot}g^{-1}$ and an area specific resistance (ASR) of 0.18–0.22 $\Omega{\cdot}cm^2$.

Visual adsorption tests were conducted by immersing electrode materials with the same area into 20 mL aqueous solutions of NaI_3 (prepared with 6 mM NaI and 1.5 mM I_2) and Na_2S_x (15 mM Na_2S_2) respectively, followed by continuous stirring at room temperature for 24 hours to ensure sufficient adsorption and equilibrium of active species on the material surfaces. UV–vis spectrophotometry was then used to record the absorption spectra of the solutions after adsorption, and the adsorption performance of different electrodes was quantitatively compared by analyzing the variation in characteristic peak intensity.

Flow battery performance tests were carried out on a NEWARE battery testing system (Shenzhen Neware Electronics Co., Ltd.). Galvanostatic charge–discharge tests were conducted at various current densities. The charging process was terminated by capacity cutoff corresponding to 100%, 50%, and 10% state of charge (SOC), with an upper voltage limit of 2.0 V for overcharge protection. The discharging process was controlled by both capacity cutoff (100%, 50%, and 10% SOC) and a low-voltage cutoff of 0.1 V. The catholyte was 2.0 M NaI + 0.5 M I_2, and the anolyte was 2.0 M Na_2S_2. The electrolyte flow rate was fixed at 10 $mL{\cdot}min^{-1}$ during all measurements. The theoretical capacity was calculated based on the catholyte (iodine component), using 5 mL of 2.0 M NaI + 0.5 M I_2, yielding a nominal capacity of 134 mAh.

Electrochemical impedance spectroscopy (EIS) tests of the assembled full cell were performed using a CHI760D electrochemical workstation. Before the test, the assembled full cell was connected to the electrolyte circulation system, and the peristaltic pump was turned on to continuously circulate the cathodic and anodic electrolytes inside the cell for 5 min. This operation ensured that both the surface and internal pores of the graphite felt electrode were fully wetted by the electrolyte, eliminating poor interfacial contact caused by insufficient wetting. After complete electrode wetting, the electrolyte circulation was stopped, and the EIS measurement was immediately conducted. The test parameters were set as follows: the frequency scanning range was from 0.1 Hz to 100 kHz, the amplitude of the AC excitation signal was 10 mV, and the test was carried out at the open-circuit potential. By collecting the impedance response at different frequencies, kinetic information including ohmic resistance, charge transfer resistance and diffusion impedance of the cell can be further analyzed.

4.3 DFT calculations

All DFT calculations were performed using the Vienna *Ab initio* Simulation Package (VASP). The exchange-correlation energy under the generalized gradient approximation (GGA) was described by the Perdew–Burke–Ernzerhof (PBE) functional. To accurately characterize the interlayer van der Waals (vdW) interactions, the DFT+D3 method with Becke–Johnson damping was adopted for correction. A plane-wave cutoff energy of 450 eV

was set in the calculations, and all atomic positions and unit cell parameters were fully relaxed until the average force on each atom converged to below 0.03 eV·Å^{-1}. The preprocessing and postprocessing of the calculation data were completed using the VASPKIT software.

Acknowledgements

This work was financially supported by the Special Fund for Science and Technology Development of Guangxi (AD25069078), the Guangxi Natural Science Fund for Distinguished Young Scholars (2024GXNSFFA010008), and the National Natural Science Foundation of China (22469002 and 22509167).

Electronic Supplementary Material Supplementary material (additional SEM, TEM, XPS, XRD characterization data, CV curves at various scan rates, electrochemical performance tests, adsorption energy tables, and performance comparison with reported catalysts) is available in the online version of this article at https://doi.org/10.26599/NRE.2026.9120260.

References

[1] Sreenath, S.; Nayanthara, P. S.; Pawar, C. M.; Ash, A.; Bhatt, B.; Verma, V.; Nagarale, R. K. An aqueous polysulfide redox flow battery with a semi-fluorinated cation exchange membrane. *Energy Adv.* **2024**, *3*, 203–214.

[2] Liu, Y. P.; Niu, Y. C.; Ouyang, X. C.; Guo, C.; Han, P. Y.; Zhou, R. C.; Heydari, A.; Zhou, Y.; Ikkala, O.; Tigranovich, G. A. et al. Progress of organic, inorganic redox flow battery and mechanism of electrode reaction. *Nano Res. Energy* **2023**, *2*, e9120081.

[3] Su, L.; Badel, A. F.; Cao, C. S.; Hinricher, J. J.; Brushett, F. R. Toward an inexpensive aqueous polysulfide-polyiodide redox flow battery. *Ind. Eng. Chem. Res.* **2017**, *56*, 9783–9792.

[4] Gao, M. Q.; Wang, Z. Y.; Lek, D. G.; Wang, Q. Towards high power density aqueous redox flow batteries. *Nano Res. Energy* **2023**, *2*, e9120045.

[5] Wang, Z. G.; Lu, G. L.; Wei, T. R.; Meng, G.; Cai, H. X.; Feng, Y. H.; Chu, K.; Luo, J.; Hu, G. Z.; Wang, D. S. et al. Synergy of single atoms and sulfur vacancies for advanced polysulfide-iodide redox flow battery. *Nat. Commun.* **2025**, *16*, 2885.

[6] Tong, X.; Sun, K. F.; Ye, H.; Cao, L.; Zhuang, J. L.; Tian, J.; Zhan, X. X. Recent advances in the high entropy materials for advanced energy storage with machine learning. *Mater. Rep.: Energy* **2025**, *5*, 100379.

[7] Yu, X. F.; Lin, Z. X.; Gao, H. G.; Wang, H. X.; Shao, D. Y.; Shi, Y. J.; Xu, J.; Huang, Y. C.; Cao, J. Y. Polysulfide-based aqueous redox flow batteries enhanced by carbon electrodes with S_8/S_x^{2-} redox pairs and hydrophilic carbon nanocuboids. *ACS Appl. Energy Mater.* **2025**, *8*, 3592–3598.

[8] Gao, M. Q.; Huang, S. P.; Zhang, F. F.; Lee, Y. M.; Huang, S. Q.; Wang, Q. Successive ionic layer adsorption and reaction-deposited copper sulfide electrocatalyst for high-power polysulfide-based aqueous flow batteries. *Mater. Today Energy* **2020**, *18*, 100540.

[9] Zhang, J. N.; Li, J.; Yu, K. F.; Wang, Q.; Zhang, H.; Zhang, F. F.; Yan, J. M. Charging-free redox flow battery for continuous high-power electricity generation from low-grade heat. *Nano Res. Energy* **2025**, *4*, e9120176.

[10] Ma, X. L.; Xu, C. G.; Yang, Y.; Sun, D.; Zhao, K.; Lu, C. B.; Jin, P.; Chong, Y. T.; Pruksawan, S.; Xiao, Z. H. et al. S-doped mesoporous graphene modified separator for high performance lithium-sulfur batteries. *Mater. Rep.: Energy* **2024**, *4*, 100279.

[11] Lan, J. J.; Zhang, S.; Yang, L.; Chen, C. J.; Wu, H. L.; Feng, L. B.; An, D. L.; Chen, J. J. High-power polysulfide redox flow batteries via an interfacial electron field on a 2D mesoporous heterojunction. *ACS Nano* **2025**, *19*, 31699–31708.

[12] Tsega, T. T.; Zai, J. T.; Lai, C. W.; Li, X. H.; Qian, X. F. Earth-abundant $CuFeS_2$ nanocrystals@graphite felt electrode for high performance aqueous polysulfide/iodide redox flow batteries. *Chin. J. Struct. Chem.* **2024**, *43*, 100192.

[13] Reddy, J.; Viswanathan, K. K.; Kandasamy, P. FeOOH@CoP/NF heterointerface catalyst for electrocatalytic water dissociation in alkaline medium. *Int. J. Hydrogen Energy* **2025**, *138*, 215–225.

[14] Li, G. L.; Jiang, F.; Zhuo, Q.; Li, Q. Y.; Zhang, S. H.; Mao, Q.; Li, H. J.; Huang, R. Y.; Zhao, Y. Optimizing OH* adsorption via Zn doping into Ni_2P/CoP heterostructures enables high catalytic activity toward alkaline hydrogen evolution reaction. *J. Mater. Chem. A* **2026**, *14*, 31382–31392.

[15] Belgibayeva, A.; Rakhatkyzy, M.; Adi, A.; Taniguchi, I. Synthesis of free-standing $Co_xP/Co_3(PO_4)_2$/C composite nanofiber mats and their characteristics as multi-functional interlayers for lithium-sulfur batteries. *ChemElectroChem* **2022**, *9*, e202200458.

[16] Ng, S. F.; Lau, M. Y. L.; Ong, W. J. Lithium-sulfur battery cathode design: Tailoring metal-based nanostructures for robust polysulfide adsorption and catalytic conversion. *Adv. Mater.* **2021**, *33*, 2008654.

[17] Du, M.; Shi, J. K.; Shi, Y. X.; Zhang, G. X.; Yan, Y.; Geng, P. B.; Tian, Z. Q.; Pang, H. Effects of O, S, and P in transition-metal compounds on the adsorption and catalytic ability of sulfur cathodes in lithium-sulfur batteries. *Chem. Sci.* **2024**, *15*, 9775–9783.

[18] Zhang, G. X.; Chen, X. R.; Yu, X. M.; Li, Q. Y.; Wang, H. Q.; Hu, S. J.; Jiang, J. T.; Huang, Y. G.; Ma, Z. L. Crystalline-amorphous heterostructure on the phosphatized P-CoS_2/CNT for augmenting the catalytic conversion kinetics of Li-S batteries. *Chem. Eng. J.* **2024**, *488*, 150696.

[19] Shen, J. D.; Xu, X. J.; Liu, J.; Liu, Z. B.; Li, F. K.; Hu, R. Z.; Liu, J. W.; Hou, X. H.; Feng, Y. Z.; Yu, Y. et al. Mechanistic understanding of metal phosphide host for sulfur cathode in high-energy-density lithium-sulfur batteries. *ACS Nano* **2019**, *13*, 8986–8996.

[20] Belgibayeva, A.; Turarova, G.; Dangaliyeva, A.; Sultanov, F.; Nurpeissova, A.; Mukanova, A.; Bakenov, Z. Polysulfide-mediating properties of nickel phosphide carbon composite nanofibers as free-standing interlayers for lithium-sulfur batteries. *RSC Adv.* **2024**, *14*, 36593–36601.

[21] Hu, X. M.; Zhang, S. L.; Sun, J. W.; Yu, L.; Qian, X. Y.; Hu, R. D.; Wang, Y. N.; Zhao, H.; Zhu, J. W. 2D Fe-containing cobalt phosphide/cobalt oxide lateral heterostructure with enhanced activity for oxygen evolution reaction. *Nano Energy* **2019**, *56*, 109–117.

[22] Gao, R.; Wang, Z. Y.; Liu, S.; Shao, G. J.; Gao, X. P. Metal phosphides and borides as the catalytic host of sulfur cathode for lithium-sulfur batteries. *Int. J. Miner. Metall. Mater.* **2022**, *29*, 990–1002.

[23] Souza, A. S.; Bezerra, L. S.; Cardoso, E. S. F.; Fortunato, G. V.; Maia, G. Nickel pyrophosphate combined with graphene nanoribbon used as efficient catalyst for OER. *J. Mater. Chem. A* **2021**, *9*, 11255–11267.

[24] Gayathri, S.; Arunkumar, P.; Saha, D.; Han, J. H. Composition engineering of ZIF-derived cobalt phosphide/cobalt monoxide heterostructures for high-performance asymmetric supercapacitors. *J. Colloid Interface Sci.* **2021**, *588*, 557–570.

[25] Orr, K. W. P.; Collins, S. M.; Reynolds, E. M.; Nightingale, F.; Boström, H. L. B.; Cassidy, S. J.; Dawson, D. M.; Ashbrook, S. E.; Magdysyuk, O. V.; Midgley, P. A. et al. Single-step synthesis and interface tuning of core-shell metal-organic framework nanoparticles. *Chem. Sci.* **2021**, *12*, 4494–4502.

[26] Osman, S.; Peng, C.; Li, F. K.; Chen, H. L.; Shen, J. D.; Zhong, Z. M.; Huang, W. J.; Xue, D. F.; Liu, J. Defect-induced dense amorphous/crystalline heterophase enables high-rate and ultrastable sodium storage. *Adv. Sci.* **2022**, *9*, 2205575.

[27] Su, Q.; Yu, L. Sub-10 nm PdNi@PtNi core-shell nanoalloys for efficient ethanol electro-oxidation. *Molecules* **2024**, *29*, 4853.

[28] He, R.; Wang, S. Q.; Yang, L. L.; Horta, S.; Ding, Y.; Di, C.; Zhang, X. S.; Xu, Y.; Ibáñez, M.; Zhou, Y. T. et al. Active site switching on high entropy phosphides as bifunctional oxygen electrocatalysts for rechargeable/robust Zn-air battery. *Energy Environ. Sci.* **2024**, *17*,

7193–7208.
[29] Zhang, Q.; Wang, Z. W.; Wang, L. H.; Wei, Z. C.; Zhuo, L. C.; Liu, Y. F.; Shakir, I.; Hu, G. Z.; Liu, X. J. Nano-hollow carbon-supported high-entropy alloy catalysts for energy-saving seawater electrolysis. *Nano Res. Energy* **2025**, *4*, e9120196.
[30] Zhou, T. T.; Cao, Z.; Tai, X. S.; Yu, L.; Ouyang, J.; Li, Y. F.; Lu, J. T. Hierarchical $Co(OH)_2$ dendrite enriched with oxygen vacancies for promoted electrocatalytic oxygen evolution reaction. *Polymers* **2022**, *14*, 1510.
[31] Wu, Q.; Gao, Q. P.; Shan, B.; Wang, W. Z.; Qi, Y. P.; Tai, X. S.; Wang, X.; Zheng, D. D.; Yan, H.; Ying, B. W. et al. Recent advances in self-supported transition-metal-based electrocatalysts for seawater oxidation. *Acta Phys.-Chim. Sin.* **2023**, *39*, 2303012.
[32] Yang, Z. Y.; Ji, Y. H.; Ren, J. L.; Wang, X. Y.; Xue, Y. J.; Tian, J. 2D/2D heterointerface engineering of $Ni_2P/ZnIn_2S_4$ photocatalysts for enhanced photocatalytic H_2 evolution. *Mater. Rep.: Energy* **2026**, *6*, 100401.
[33] Wu, Q.; Li, J.; Wu, T. W.; Ji, L.; Zhang, R.; Jiang, P. F.; Chen, H. Y.; Zhao, R. B.; Asiri, A. M.; Sun, X. P. One-step preparation of cobalt-nanoparticle-embedded carbon for effective water oxidation electrocatalysis. *ChemElectroChem* **2019**, *6*, 1996–1999.
[34] Liu, X. H.; Zhang, L. R.; Ma, X. Z.; Lu, H. Q.; Li, L.; Zhang, X. T.; Wu, L. L. Conversion of polysulfides on core-shell CoP@C nanostructures for lithium-sulfur batteries. *Chem. Eng. J.* **2023**, *454*, 140460.
[35] Zhang, H.; Feng, Z. Y.; Ding, T. H.; Song, B.; Lu, K.; Yang, C. C.; Jiang, Q. Mn-Co dual-metal single-atom catalytic sites for boosted redox kinetics in aqueous polysulfide/ferricyanide flow batteries. *Nano Lett.* **2025**, *25*, 11051–11059.
[36] Lin, P. X.; Chen, G. H.; Kang, Y. H.; Zhang, M. H.; Yang, J.; Lv, Z. H.; Yang, Y.; Zhao, J. B. Simultaneous inhibition of Zn dendrites and polyiodide ions shuttle effect by an anion concentrated electrolyte membrane for long lifespan aqueous zinc-iodine batteries. *ACS Nano* **2023**, *17*, 15492–15503.
[37] Ma, D.; Hu, B.; Wu, W. D.; Liu, X.; Zai, J. T.; Shu, C.; Tadesse Tsega, T.; Chen, L. W.; Qian, X. F.; Liu, T. L. Highly active nanostructured CoS_2/CoS heterojunction electrocatalysts for aqueous polysulfide/iodide redox flow batteries. *Nat. Commun.* **2019**, *10*, 3367.
[38] Wang, H.; Jamil, S.; Fasehullah, M.; Bao, S. J.; Li, Y.; Xu, M. W. Novel N-doped carbon nanotubes impregnated Mn spheres with polydopamine coating as an efficient polysulfide immobilizer for Li-S batteries. *Mater. Rep.: Energy* **2024**, *4*, 100298.
[39] Miao, K. J.; Chen, S. L.; Zhou, J. Q. Structure-engineered amorphous MoS_3 catalysts for enhanced sulfur conversion kinetics in wide-temperature lithium-sulfur batteries. *Mater. Rep.: Energy* **2026**, *6*, 100405.
[40] Zhu, Y.; He, K.; Tadesse Tsega, T.; Ali, N.; Zai, J. T.; Huang, S. S.; Qian, X. F.; Chen, Z. W. Cu_2CoGeS_4 nanocrystals for high performance aqueous polysulfide/iodide redox flow batteries: Enhanced selectively towards the electrocatalytic conversion of polysulfides. *Sustain. Energy Fuels* **2020**, *4*, 2892–2899.
[41] Elgrishi, N.; Rountree, K. J.; McCarthy, B. D.; Rountree, E. S.; Eisenhart, T. T.; Dempsey, J. L. A practical Beginner's guide to cyclic voltammetry. *J. Chem. Educ.* **2018**, *95*, 197–206.
[42] Li, L. Y.; Yan, S.; Huang, Y. J.; Zhong, F. F.; Cao, J. C.; Ding, M.; Jia, C. K. Carbon felt electrode coated with WS_2 enables a high-performance polysulfide/ferricyanide flow battery. *Rare Met.* **2024**, *43*, 5039–5047.
[43] Zhang, X. H.; Liu, L. S.; Zhang, K. Y.; Zhang, D. H.; Hou, S. Y.; Zhao, J. L.; He, H. X.; Wu, X. L.; Liu, J. G.; Yan, C. W. Modulating single-atom sulfur-vacancy defect in MoS_{2-x} catalysts to boost cathode redox kinetics for vanadium flow batteries. *Energy Storage Mater.* **2024**, *69*, 103442.
[44] Chen, S. M.; Chen, L. K.; Tian, N.; Hu, S. N.; Yang, S. L.; Shen, J. F.; Tang, J. X.; Wu, D. Y.; Chen, M. S.; Zhou, Z. Y. et al. Double-shell confinement strategy enhancing durability of PtFeTi intermetallic catalysts for the oxygen reduction reaction. *ACS Catal.* **2024**, *14*, 16664–16672.
[45] Gao, X. Q.; Cao, L. L.; Chang, Y.; Yuan, Z. M.; Zhang, S. X.; Liu, S. J.; Zhang, M. T.; Fan, H.; Jiang, Z. Y. Improving the CO_2 hydrogenation activity of photocatalysts via the synergy between surface frustrated Lewis pairs and the CuPt alloy. *ACS Sustainable Chem. Eng.* **2023**, *11*, 5597–5607.
[46] Luo, M. C.; Yang, Y.; Guo, S. J. Core-shell architecture advances oxygen electrocatalysis. *Chem* **2019**, *5*, 260–262.
[47] Li, Q. R.; Wan, G.; Zhao, W. P.; Yang, C.; Peng, C. L.; Duan, Z. L.; Chen, H. R. Probing nitrogen-doping effects in the core-shell structured catalysts for bifunctional electrocatalysis. *ChemCatChem* **2018**, *10*, 4248–4252.
[48] Luo, Y. F.; Luo, N. N.; Kong, W. B.; Wu, H. C.; Wang, K.; Fan, S. S.; Duan, W. H.; Wang, J. P. Multifunctional interlayer based on molybdenum diphosphide catalyst and carbon nanotube film for lithium-sulfur batteries. *Small* **2018**, *14*, 1702853.
[49] Nie, R.; Nie, Y. Z.; Wu, J. J.; Yu, L. H.; Liu, L.; Xi, J. Y. An aqueous alkaline zinc-sulfur flow battery. *Chem. Commun.* **2024**, *60*, 2946–2949.
[50] Lu, G. L.; Zhang, J. W.; Wang, Z. W.; Wang, Z. G.; Feng, Y. H.; Hu, C. J.; Zhuo, L. C.; Liu, X. J. Sulfur vacancy-rich MoS_2 anchored oxidized graphene as advanced catalysts for polysulfide-iodine redox flow battery. *Chin. Chem. Lett* **2026**, *37*, 111650.
[51] Yan, L. T.; Shao, Y. Y.; Wang, W. A hydrogen iron flow battery with high current density and long cyclability enabled through circular water management. *Energy Environ. Mater.* **2023**, *6*, e12478.
[52] Xiao, M.; Di, H. S.; Liu, Z. Q.; Bai, Y. S.; Ran, R.; Zhou, W.; Yang, G. M.; Shao, Z. P. High-entropy strategies transforming solid oxide cells: Progress and perspectives. *Mater. Rep.: Energy* **2026**, *6*, 100400.